Macromolecules
ARTICLE

Macromolecules **2009**, *42*, 4887–4895 **4887**
DOI: 10.1021/ma900250y

Mechanical Properties of Glassy Polyethylene Nanofibers via Molecular Dynamics Simulations

Sezen Buell,[†] Krystyn J. Van Vliet,[†] and Gregory C. Rutledge*,[‡]

[†]*Department of Materials Science and Engineering and* [‡]*Department of Chemical Engineering, Massachusetts Institute of Technology, Cambridge, Massachusetts 02139*

Received February 4, 2009; Revised Manuscript Received April 25, 2009

ABSTRACT: The extent to which the intrinsic mechanical properties of polymer fibers depend on physical size has been a matter of dispute that is relevant to most nanofiber applications. Here, we report the elastic and plastic properties determined from molecular dynamics simulations of amorphous, glassy polymer nanofibers with diameter ranging from 3.7 to 17.7 nm. We find that, for a given temperature, the Young's elastic modulus E decreases with fiber radius and can be as much as 52% lower than that of the corresponding bulk material. Poisson's ratio ν of the polymer comprising these nanofibers was found to decrease from a value of 0.3 to 0.1 with decreasing fiber radius. Our findings also indicate that a small but finite stress exists on the simulated nanofibers prior to elongation, attributable to surface tension. When strained uniaxially up to a tensile strain of $\varepsilon = 0.2$ over the range of strain rates and temperatures considered, the nanofibers exhibit a yield stress σ_y between 40 and 72 MPa, which is not strongly dependent on fiber radius; this yield stress is approximately half that of the same polyethylene simulated in the amorphous bulk.

Introduction

Mechanical properties of polymeric nanostructures are of critical importance in a wide variety of technological applications. In particular, polymer nanofiber-based nonwoven materials are subject to different forces and deformations in applications such as filtration media,[1] tissue engineering,[2] biomedical applications,[3] composites,[4] and other industrial applications.[5] Such applied forces and resulting displacements may result in permanent deformation and eventually mechanical failure of individual nanofibers. The properties of the nonwoven materials are convoluted functions of the inherent properties of these fibers as well as the organization of and interactions among fibers within the nonwoven material. Therefore, it is desirable to determine independently the mechanical properties of single nanofibers.

In recent years, various attempts have been made to quantify the elastic properties of isolated polymer fibers of diameter $d <$ 1 μm via direct experimental measurements.[6−17] Mechanical characterization techniques that have been developed to test individual polymer fibers include uniaxial tensile loading as well as bending and indentation of individual fibers using atomic force microscopy (AFM) cantilevered probes to impose deformation. For example, the effects of processing conditions on mechanical properties of electrospun poly(L-lactide) (PLLA) nanofibers with diameters of 610 and 890 nm were investigated via tensile testing.[7] Higher rotation rate of the collection roller correlated with higher tensile Young's elastic modulus E and strength of the nanofibers, which was attributed to the ordered structure developed during the collection process.[7] Bellan et al. measured the Young's elastic moduli of poly(ethylene oxide) (PEO) fibers with diameters 80 nm $< d <$ 450 nm using an AFM cantilevered probe to deflect the suspended fibers and reported E in significant excess of that reported for bulk PEO.[8] The authors attributed this enhanced stiffness to the molecular orientation of PEO chains within the fibers.[8] Tensile testing of poly(ε-caprolactone) (PCL) nanofibers with diameters 1.03 μm $< d <$ 1.70 μm to the point of mechanical failure showed that fibers of smaller diameter exhibited higher fracture strength but lower ductility (strain to failure).[10] Mechanical properties of single electrospun nanofibers composed of PCL and poly(ε-caprolactone-*co*-ethylethylene phosphate) (PCLEEP) were also measured under uniaxial tension, indicating an increase in both stiffness and strength as the fiber diameter decreased from 5 μm to ~250 nm.[11] Chew et al. also found that E of these PCL nanofibers were at least twice that of PCL thin films of comparable thickness.[11] Recently, Wong et al. reported an abrupt increase in tensile strength and stiffness of these PCL fibers below fiber diameter of 1.4 μm and attributed this to improved crystallinity and molecular orientation in fibers of smaller diameter.[12] Young's moduli of electrospun nylon-6 nanofibers were found to increase from 20 to 80 GPa as the fiber diameter decreased from 120 to 70 nm.[13] In separate tensile studies on electrospun nylon-6,6 nanofibers, E was reported to increase 3-fold for fibers with diameters $<$500 nm.[16] No significant increase in degree of crystallinity or chain orientation accompanied this increase in E.[16] Using scaling arguments, these authors reasoned that this size-dependent stiffening effect was due to the confinement of a supramolecular structure, consisting of molecules with correlated orientation, comparable to the nanofiber diameter. Finally, the shear elastic modulus G of glassy electrospun polystyrene (PS) fibers of 410 nm $< d <$ 4 μm was estimated using an AFM probe via shear modulation force spectroscopy of the fiber surface and also reported to increase with decreasing fiber diameter.[17] This trend was attributed to molecular chain alignment frozen in during the electrospinning process. When functionalized clay was added to these PS nanofibers, G of the fibers was further increased, although the stiffening mechanism remains unclear.[17] Importantly, although these reports generally indicate increasing elastic modulus and strength with decreasing fiber diameter, all of these fibers (with the exception of the PS fibers of ref 17) are also semicrystalline.

Although these experimental methods can provide information on the Young's elastic modulus, E, yield strength, σ_y, and fracture strength, σ_f, of nanofibers, several challenges exist that

*Corresponding author. E-mail: rutledge@mit.edu.

limit the precision and accuracy of these mechanical property measurements. These challenges include the required force resolution, the difficulty of preparing, isolating, and manipulating such small fibers without compromising them, and the dearth of suitable modes of imaging or displacement measurements that do not damage the fibers. Because of these difficulties, to the best of our knowledge, experimental data are not available for the elastic or plastic properties of polymer nanofibers with diameters less than 50 nm. Therefore, it is not yet clear if the stiffening and strengthening effects described above are peculiar to fibers in the range of diameters from ~70 to 500 nm or if these trends would persist to even smaller length scales. Molecular scale simulations can provide valuable insights to help predict and understand the mechanical behavior of such small-scale structures and to identify any emergent behavior that is a consequence of their nanoscale dimensions.

For example, it has been argued by several independent research groups that physical measurements correlated with the glass transition temperature T_g indicate a difference between T_g of amorphous polymeric thin films and bulk counterparts.[18−23] The results of these studies suggest the existence of a region of increased macromolecular mobility near the surface of free-standing, glassy polymer films or membranes. Through molecular dynamics simulations of amorphous polyethylene, we have shown that the depression of the glass transition temperature may also be observed for polymer nanofibers.[24] Invoking a simple layer model, the reduced T_g can be rationalized by the assumption that the surface of the polymer nanofibers exhibits increased molecular mobility. The presence of this outer "layer" of enhanced mobility, which is more accurately a gradient material of finite thickness located at the free surface, might modulate the capacity of the material to sustain applied loads and thus affect the measured mechanical properties of both polymeric thin films and nanofibers. Another important parameter in determining the mechanical properties of these structures is the ambient temperature, since both structural and mechanical properties can change significantly in polymers as the glass transition temperature is approached.

Previous computational simulations of amorphous (glassy) polymeric, prismatic cantilevered plates adhered to a substrate have shown that the overall bending modulus of the plate remains comparable to bulk materials, until the width of the plates approaches a critical value of 20σ, where σ is the diameter of the coarse-grained polymer segments.[25,26] Below the critical plate width, the bending modulus decreases with decreasing width and can be significantly smaller than that of the bulk polymer. Workum et al.[26] showed that the material in the surface region comprises a significant fraction of the entire width of the plate, so that deviations from bulk behavior can be significant. Nonequilibrium molecular dynamics simulations using a coarse-grained polymer model showed that compliant layers form near the free surfaces of glassy thin films.[27] These authors also calculated that the ratio of the surface layer thickness increased to more than half of the entire film thickness as the temperature approached the T_g of the bulk polymer.[27] Although two studies of the structural and physical properties of simulated, glassy polymer nanofibers have been reported to date, mechanical properties of such fibers have not been calculated.[28,29] However, experimental studies of amorphous polymer thin films suggest that the stiffnesses of PS or poly(methyl methacrylate) (PMMA) thin films of thickness < 40 nm on poly(dimethylsiloxane) (PDMS) substrates, as inferred from elastic buckling of the adhered films, are significantly less than those of bulk counterparts.[30,31] This behavior was explained by applying a composite model that consisted of a compliant surface layer of reduced elastic modulus and a bulklike region at the film center.[31] Wafer curvature experiments have also indicated that the biaxial elastic modulus of PS thin films of 10 nm thickness is an order of magnitude smaller than that of the corresponding bulk PS.[32]

Experiments and simulations therefore suggest that mechanical properties of polymer nanostructures (i.e., free-standing or adherent thin films of nanoscale thickness and fibers of nanoscale diameter) can deviate significantly from that of the bulk polymer counterparts, but with very different trends. Whereas the properties of adherent thin films depend strongly on the substrate to which the film is adhered, free-standing films and fibers might be expected to behave more similarly. Given these discrepancies, the fundamental questions addressed in this work are (1) whether the elastic and plastic properties of simulated, amorphous polymer nanofibers are indeed different from those of the bulk material or thin film counterparts, and (2) if these properties in fact differ from bulk predictions, how this deviation depends on the fiber dimensions for fiber radii < 10 nm. We begin our discussion by describing the modeling and simulation techniques used to determine the elastic properties of the material, namely E and ν. We discuss the effect of surface tension on the axial force−elongation response of nanofibers at low strain. We then report results for elastic properties as a functions of fiber radius R_{fiber} and temperature and interpret them using a simple layer model. We also report the characterization of σ_y and postyield behavior as functions of nanofiber radius and temperature.

Simulation Model and Method

A. Model. All simulations reported here were conducted using a large-scale atomic/molecular massively parallel simulator (LAMMPS).[33] LAMPPS is a molecular dynamics code that efficiently processes intermolecular interaction potentials for compliant materials such as polymers and incorporates message-passing techniques and spatial decomposition of the simulation domain on parallel processors typical of state-of-the-art Beowulf clusters. We employ a united atom model for polyethylene (PE), described originally by Paul et al.[34] with subsequent modifications by Bolton et al.[35] and In't Veld and Rutledge.[36] This is the same force field that we used previously to characterize structural and thermal properties of polyethylene nanofibers.[24] The functional form and parameters of the force field are given as

$$E_{\text{bond}} = k_b(l - l_0)^2 \tag{1}$$

$$E_{\text{angle}} = k_a(\theta - \theta_0)^2 \tag{2}$$

$$E_{\text{torsion}} = \sum_{i=1}^{3} \frac{1}{2} k_i [1 - \cos i\phi] \tag{3}$$

$$E_{\text{LJ}} = 4\varepsilon\left[\left(\frac{\sigma}{r}\right)^{12} - \left(\frac{\sigma}{r}\right)^{6}\right] \tag{4}$$

where $k_b = 1.464 \times 10^5$ kJ/(mol nm^2), $l_0 = 0.153$ nm, $k_a = 251.04$ kJ/(mol deg^2), $\theta_0 = 109.5°$, $k_1 = 6.77$ kJ/mol, $k_2 = -3.627$ kJ/mol, and $k_3 = 13.556$ kJ/mol. The nonbonded potential parameters are $\varepsilon(CH_2{-}CH_2) = 0.391$ kJ/mol, $\varepsilon(CH_3{-}CH_3) = 0.948$ kJ/mol, $\varepsilon(CH_2{-}CH_3) = 0.606$ kJ/mol, and $\sigma = 0.401$ nm (for all united atom types). The nonbonded interactions were truncated at a distance of 1 nm and were calculated between all united atom pairs that were located on two different molecular chains or that were separated by four or more bonds on the same chain.

Since we implemented a united atom force field, the prototypical PE nanofibers are composed of methyl and methylene groups only, wherein the hydrogen atoms are lumped together with the carbon atoms. We simulated two different molecular weights, where each polymer chain within the fiber has either 100 carbon atoms (C100) or 150 carbon atoms (C150) on the backbone. The size of the representative volume element (i.e., simulation box) of these simulated systems thus ranged from 1500 carbons to 150 000 carbons. Using the Gibbs dividing surface method to determine the fiber diameter, as described previously,[24] these systems corresponded to fibers of diameter 3.7 nm $< d <$ 17.7 nm at a simulated temperature $T = 100$ K.

B. Simulation Methods. Free-standing PE nanofibers were prepared in a two-step molecular dynamics (MD) scheme as explained in more detail previously.[24] In the first step, the cubic simulation box was equilibrated using periodic boundary conditions at 495 K, which is above the melting temperature of PE. The initial density within the simulation box was 0.75 g/cm^3.

To determine the mechanical properties of solid PE nanofibers, we next cooled bulk structures from 495 to 100 K with an effective cooling rate of 1.97×10^{10} K/s. The glass transition temperature (T_g) for bulk amorphous PE described by this force field has been previously estimated to be 280 K,[37] and T_g of the surface layer was estimated to be 150 K.[24] We used an *NPT* ensemble with a constant, isotropic pressure of $P = 10^5$ Pa during cooling. We saved configurations at three different temperatures (100, 150, and 200 K) for determination of bulk mechanical properties and subsequently used these configurations to construct nanofibers. In this second step, the simulation box dimensions were increased simultaneously in two directions (i.e., x and y) without rescaling coordinates, such that the system no longer interacted with its images in these directions. The box dimension was unchanged in the third direction (i.e., z). Upon subsequent relaxation in the NVT ensemble for 10 ns at the desired temperature, the system reduced its total energy by forming a cylindrically symmetric free surface concentric with the z-axis of the box. The resulting nanofiber was fully amorphous and periodic along the z-direction. Measurement of the local order parameter $P_2 = (3 \cos^2 \theta_i - 1)/2$, where θ_i is the angle between the z-axis and the vector from bead $i-1$ to bead $i+1$, revealed no significant orientational order within the fibers, other than a very weak tendency for chain ends to orient perpendicular, and middle segments parallel, to the fiber surface. The bulk configurations at 100, 150, and 200 K were also equilibrated in the *NPT* ensemble, with the usual periodic boundary conditions in x, y, and z, before deformation to determine the bulk mechanical properties.

Deformation of fibers was simulated by controlling the displacement of the z dimension of the simulation box to induce uniaxial deformation parallel to the fiber axis (Figure 1a); the free surfaces of the fibers were unconstrained. Deformation of the bulk configurations was simulated by rescaling one dimension of the simulation cell, while allowing the other two orthogonal dimensions to fluctuate in response to the barostat, as described in detail in Capaldi et al.[37] The resulting strain rate for all temperatures ranged from 2.5×10^8 to 10^{10} s^{-1}. For the fibers, results are presented initially in the form of applied force vs strain, since converting force to stress requires an assumption regarding the cross-sectional area of the fibers. As argued previously,[38] defining the cross-sectional area requires a subjective decision, the effect of which becomes significant when the material dimensions are reduced to a length scale

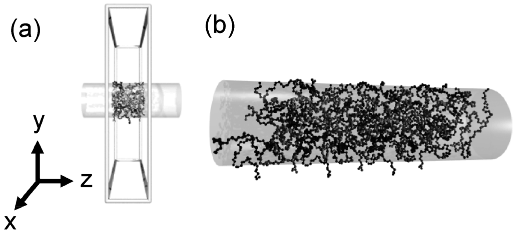

Figure 1. (a) Side view of a 30xC150 PE nanofiber obtained at the end of the *NVT* equilibration step, with the frame of the simulation cell and a cylinder corresponding to the approximate fiber diameter and orientation rendered for clarity. The simulation cell includes 30 molecules, each having 150 carbon atoms, and has a radius $R_{\mathrm{fiber}} = 2.8$ nm at 100 K according to the Gibbs dividing surface method.[24] (b) An enlarged view of the simulated fiber, with the three periodic images along the fiber axis shown. Both images were rendered using POV-Ray v3.6 ray-tracing software.[39]

comparable to the size of the particles themselves (~1 nm); different methods for defining the diameter of a fiber can thus lead to significant differences in the value of stress obtained. Samples were deformed in both compression and tension up to a strain $\varepsilon = \pm 0.05$, which is in the linear elastic deformation range at temperatures of 100 and 150 K, as confirmed by the linearity of the computed force−strain response over this range. In the case of 200 K simulations, the force−strain response was linear only up to a strain $\varepsilon =$ 0.02. To improve the signal-to-noise ratio in the computed virial equation for forces acting on the fiber (for small systems), four different initial configurations were simulated under identical conditions, and the resulting force−strain curves were averaged. Where necessary to compute stress, we invoked the Gibbs dividing surface (GDS) to define the diameter of the fibers, as described previously.[24] Young's elastic modulus was calculated from the slope of the stress−strain response in the linear elastic regime. We also studied the plastic deformation behavior of both bulk and nanofibers by continuing deformation up to a total strain $\varepsilon = 0.2$ at 100 and 150 K with a constant strain rate of 10^9 s^{-1}. For each simulation, data for force vs strain during plastic deformation were averaged over a strain interval of 0.002. The axial force on the fiber at yield was calculated from the intersection of two lines, the first being fit to the force−strain curve in the low-strain, elastic deformation region and the second being fit to the force−strain curve in the plastic deformation region; yield stress was thus computed as the force at yield (intersection of these piecewise linear fits) normalized by the GDS-defined cross-sectional area of the fiber.

Results

A. Effect of Surface Tension on Stress. Table 1 summarizes the simulated systems. In this table, chain length is the number of carbon atoms in one chain, N is the total number of atoms in the system, L is the length of the simulation box, and R_{fiber} is the radius of the nanofibers calculated by the GDS method.

Figure 2 shows the force−strain response of a nanofiber that was deformed uniaxially at 100 K. A closer inspection of this figure reveals that the force does not decrease to zero at zero applied strain. This is a feature of the nanofibers that is also suggested by continuum mechanics to be a consequence of surface tension.[40] Simulations of bulk systems (i.e., periodic boundary conditions in x, y, and z with no free surfaces) confirm that the force−strain responses indeed passes through the origin in this case.

Table 1. Chain Length and Radius Values, Determined via the GDS Method, for Simulated PE Nanofibers at All Temperatures Considered in This Study

chain length	N	L at 100 K (nm)	R_{fiber} at 100 K (nm)	L at 150 K (nm)	R_{fiber} at 150 K (nm)	L at 200 K (nm)	R_{fiber} at 200 K (nm)
C100	1 500	3.39	1.848	3.40	1.875	3.47	2
C100	3 000	4.27	2.312	4.29	2.371	4.34	2.4
C150	4 500	4.88	2.762	4.90	2.794	4.93	2.81
C100	15 000	7.29	4.1	7.33	4.148	7.38	4.2
C100	50 000	10.92	6.15	10.98	6.2	11.02	6.21
C100	100 000	13.75	7.71	13.79	7.75	13.84	7.76
C150	150 000	15.75	8.84	15.80	8.94	15.87	8.96

To investigate the finite force that is observed in the force–strain response, we calculated the instantaneous force tensor for equilibrated nanofibers (i.e., no elongation/compression) from the virial tensor W as

$$f = -\frac{1}{L_{\text{fiber}}}\Big[\sum_{i=1}^{N_{\text{bond}}} W_{\text{bond},\,ij} + \sum_{i=1}^{N_{\text{angle}}} W_{\text{angle},\,i} + \sum_{i=1}^{N_{\text{dihed}}} W_{\text{dihed},\,i} + \sum_{i=1}^{N_{\text{atom}}-1}\ \sum_{j=i+1}^{N_{atom}} W_{\text{LJ},\,ij} + \sum_{i=1}^{N_{\text{atom}}} W_{\text{kinetic}}\Big] \quad (5)$$

where L_{fiber} is the length of the fiber. Equation 5 is the summation of all contributions due to bond stretching, bond angle bending, bond torsion, Lennard-Jones interactions, and kinetic contributions. The explicit expressions of the virial contributions can be found elsewhere.[36,41] We calculated the force tensor in cylindrical coordinates, appropriate to the geometry of the fibers. Figure 3 shows the radial force f_{rr} as a function of distance from the fiber center. For this analysis, the fiber was divided into concentric cylindrical shells, starting from the fiber axis. The virial contributions were summed for the atoms that belonged to the same cylindrical shell. To translate the results for f_{rr} into radial stress σ_{rr}, we define R_{fiber} according to the GDS method.[24] The radial stress is given by

$$\sigma_{\text{rr}} = \frac{f_{\text{rr}}}{\pi R_{\text{fiber}}^{2}} \quad (6)$$

The surface tension can be calculated by integrating the radial stress σ_{rr} as follows:

$$\gamma = \int_0^{\infty} \sigma_{\text{rr}}\, \mathrm{d}r \quad (7)$$

Figure 4 shows the magnitude of surface tension calculated from eq 7 as a function of fiber radius. The error bars represent the standard deviation for the four different configurations simulated.

Here, we can also explore the validity of the continuum theory and Young–Laplace equation for small diameter fibers.[40] This equation can be written as follows for a cylinder:

$$\sigma_{zz} = \frac{\gamma}{R_{\text{fiber}}} \quad (8)$$

where γ is surface tension and R_{fiber} is the fiber radius. This relation suggests that there is a finite stress on the nanofibers due to the contribution of surface tension, even in the absence of elongation or applied force. The relative contribution of this finite stress term naturally increases as the fiber radius decreases.

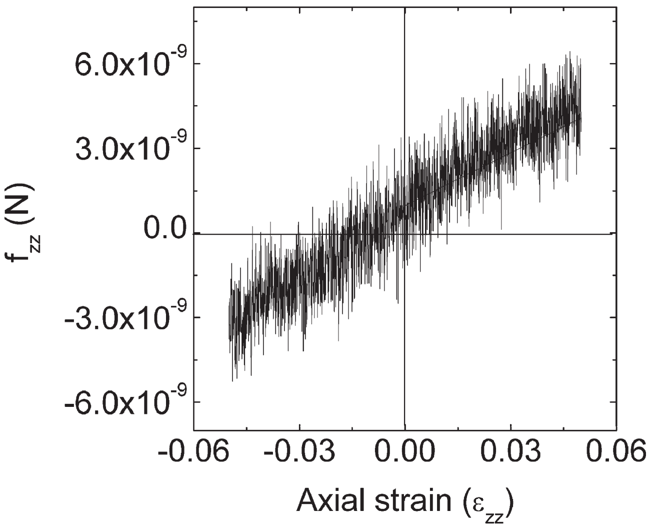

Figure 2. Force along the axial direction (f_{zz}) as a function of axial strain (ε_{zz}) in the elastic regime for a nanofiber with $N/L = 2057.61$ united atoms per nm of fiber length ($R_{\text{fiber}} = 4.1$ nm by the GDS method) at 100 K.

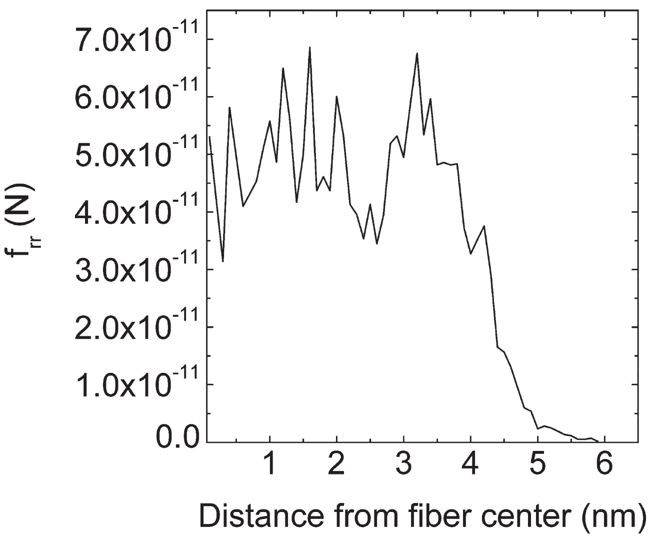

Figure 3. Radial force profile extending from the fiber core to the free surface enables the calculation of radial stress ($R_{\text{fiber}} = 4.1$ nm by the GDS method at 100 K).

Since we calculated both σ_{rr} and σ_{zz} directly from the virial equation of atomistic interactions as detailed above, we can calculate a second estimate of the surface tension γ, subject to the validity of eq 8. Estimates of γ using eqs 6 and 8 agree within 1 mN/m. These estimates from computational simulations also compare well with an experimental estimate of 44.7 mN/m for amorphous polyethylene at 100 K, obtained

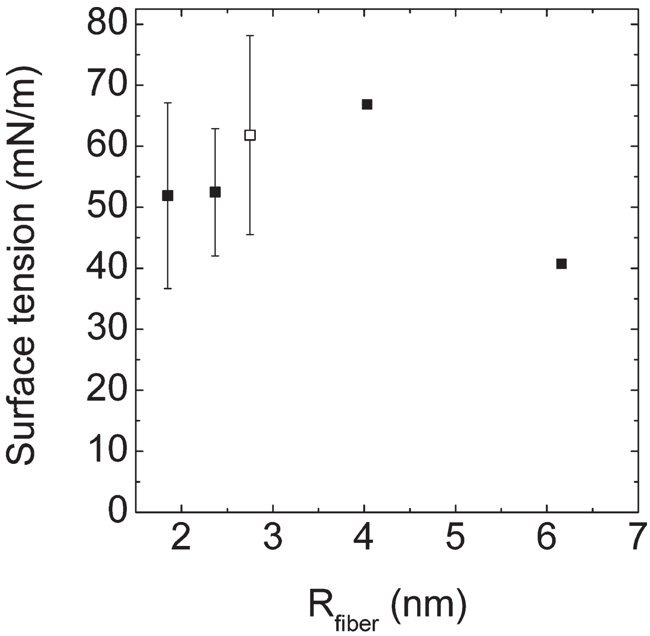

Figure 4. Surface tension as a function of R_{fiber}, as calculated from the radial component of the stress tensor at 100 K. Solid squares represent systems with chain length C100; open squares represent systems with chain length C150.

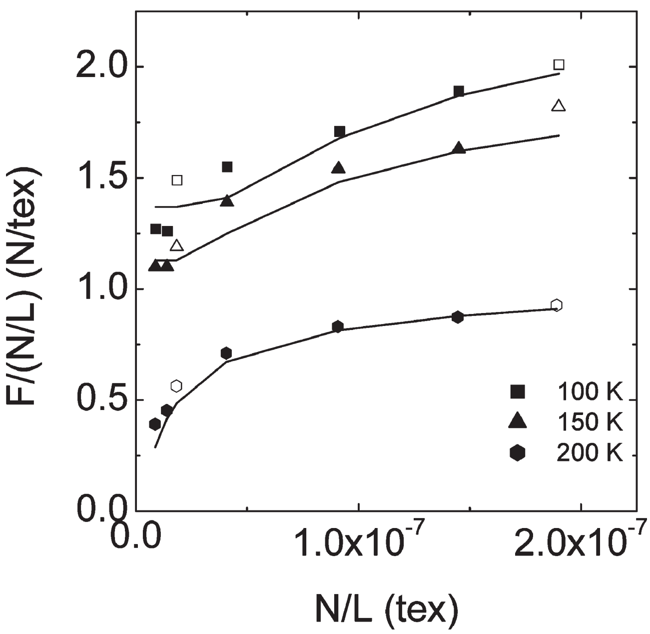

Figure 5. Dependence of $F/(N/L)$ on fiber parameter N/L at three different temperatures: 100, 150, and 200 K and at a strain rate of 2.5×10^8 s^{-1}. See text for details. Solid symbols represent systems with chain length C100; open symbols represent systems with chain length C150.

by extrapolation from the experimentally measured surface tension of a polyethylene melt between 423 and 473 K.[42] These results confirm that the source of the finite stress at zero elongation is the surface tension and that the continuum theory is capable of accounting for this phenomenon even at these very small length scales.

B. Elastic Deformation. From the slope of force vs strain ($f_{zz}-\varepsilon$ response) in the elastic regime (Figure 2), under uniaxial tension and compression parallel to the fiber long axis, we compute the quantity F, which has units of force and

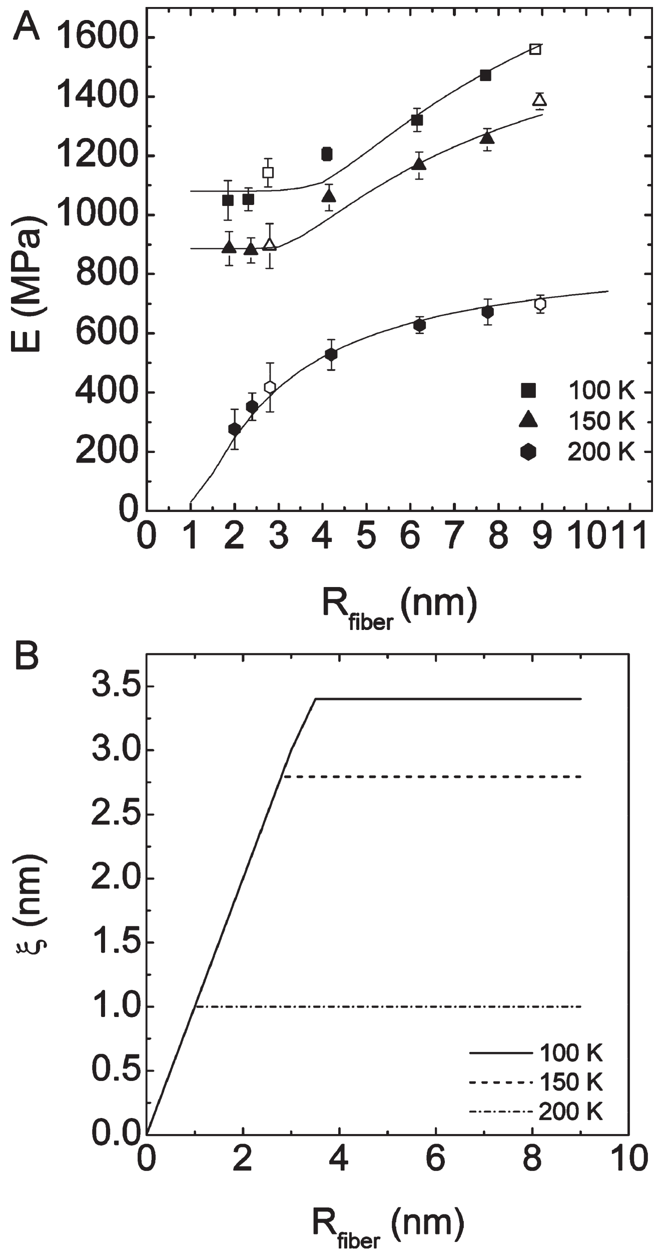

Figure 6. (A) E vs R_{fiber} at 100, 150, and 200 K and at a strain rate of 2.5×10^8 s^{-1}. The data points represent simulation data; the solid lines show the best fit to the composite model described in the text. Symbols are the same as in Figure 5. The reasonable fit of the data at larger R_{fiber} indicates that the mechanical behavior is well-described by a mechanically effective surface layer of constant thickness. (B) ξ vs R_{fiber} at 100, 150, and 200 K suggests that the mechanically effective surface layer thickness decreases with increasing temperature.

is related to the elastic modulus through the cross-sectional area, $F = EA$.

Figure 5 shows the quantity $F/(N/L)$ as a function of N/L at 100, 150, and 200 K. N is the number of atoms in the simulation, and L is the length of the simulation box along the z direction (the fiber axis). Thus, N/L is proportional to the linear density (mass per unit length) of the fiber, which is conventionally expressed in units of tex in the fiber industry; tex is the mass in g of 1 km of fiber. $F/(N/L)$ is proportional to the specific modulus of the fiber (E/ρ, where ρ is the density of the fiber) and is conventionally expressed in units of N/tex. The use of fiber industry units here avoids the need to introduce a definition for fiber radius in order to characterize the fiber deformation behavior. All three temperatures are below the glass transition of bulk PE (280 ± 30 K[37]) and were chosen to bracket the glass transition temperature estimated for the surface of these fibers (150 K[24]). As can be seen from this figure, the specific modulus $F/(N/L)$ decreases with decreasing N/L for all temperatures considered. The specific modulus for fibers of various sizes at 150 K are slightly lower than those at 100 K; between 150 and 200 K, the specific modulus drops significantly. This is an indication of the increased compliance of the surface layer within this temperature range, which contributes noticeably in nanofibers of diameter $d < 40$ nm.

In order to interpret these results for deformation of nanofibers in terms of deviation from bulklike behavior, it is necessary to compute the Young's modulus, E. For this purpose, we reintroduce R_{fiber}, defined using the GDS method. Figure 6a shows E as a function of R_{fiber}. By simulation, we determined the Young's modulus of the bulk PE E_{bulk} to be 2360, 1838, and 900 MPa at 100, 150, and 200 K, respectively, under an applied strain rate of 2.5×10^{8} s^{-1}. At a strain rate of 1×10^{10} s^{-1}, E_{bulk} was found to increase to 2758, 2490, and 1800 MPa at the same three temperatures, respectively. This strain rate dependence of E for simulated bulk PE below the glass transition has been noted previously.[43] It is likely that some relaxation mechanisms in the glassy state are suppressed at the higher strain rate. Nevertheless, the main finding—that decreasing fiber size results in increasing compliance—is relatively insensitive to strain rate, so we report further results only for the lower simulated strain rate. For all three temperatures, the Young's moduli of the fibers are lower than those of the corresponding bulk configurations.

To explain the dependence of Young's modulus on the fiber radius, we make use of composite material theory. We assume that the core of the fiber consists of bulklike material with a Young's modulus equal to that of the bulk E_{bulk} and a surface region that is more compliant, with $E_{\text{surf}} < E_{\text{bulk}}$. Assuming uniform strain throughout the fiber (i.e., the Voigt limit for material composites), we have

$$E = E_{\text{bulk}} f_{\text{bulk}} + E_{\text{surf}} f_{\text{surf}} \tag{9}$$

where E is the calculated elastic modulus of the fiber, f_{bulk} is the volume fraction of the bulklike core, and $f_{\text{surf}} = 1 - f_{\text{bulk}}$ is the volume fraction of the surface layer. The core volume fraction f_{bulk} can be written as

$$f_{\text{bulk}} = \left(1 - \frac{\xi}{R_{\text{fiber}}}\right)^2 \tag{10}$$

where ξ is the thickness of the mechanically effective surface layer; this parameter characterizes the length scale over which the elastic response of the fiber varies. ξ was further assumed to depend only on temperature; for fibers of radius less than ξ, we set $\xi = R_{\text{fiber}}$.

We used best fits of eqs 9 and 10 to our simulated results to determine values for both ξ and E_{surf} at each temperature, as shown in Figure 6a. According to eqs 9 and 10, the effective Young's modulus of the fibers should approach E_{surf} for fibers with small radii, on the order of ξ or less, and should asymptotically approach to E_{bulk} for fibers much larger than ξ. For the range of fiber radii simulated, the approach to E_{surf} around $R_{\text{fiber}} = \xi$ is accurately captured at 100 and 150 K, while the approach to E_{bulk} at large R_{fiber} is observed at 200 K. Figure 6b indicates the dependence of ξ on R_{fiber} at all three temperatures. From the fit to the two-layer composite model, we obtain values for E_{surf} of 1050, 890, and 30 MPa at temperatures of 100, 150, and 200 K, respectively. For ξ, we obtain values (at sufficiently large fiber radius R_{fiber}) of 3.4, 2.8, and 1.0 nm at temperatures of 100, 150, and 200 K, respectively. In other words, both the elastic modulus and the thickness of the mechanically effective surface layer decrease as the temperature increases from below to above the glass temperature of the surface layer.

Enhanced surface mobility of glassy polymer thin films and nanostructures has been demonstrated by several experiments[21,44] and simulations.[26,45] As the dimensions of the nanostructures decrease, the surface-to-volume ratio increases, and thus the amount of material at the surface becomes a more significant volume fraction of the entire structure, and is reflected in the overall properties. The increased mobility at the surface can cause significant stress relaxations in the mechanically effective surface layer quan-

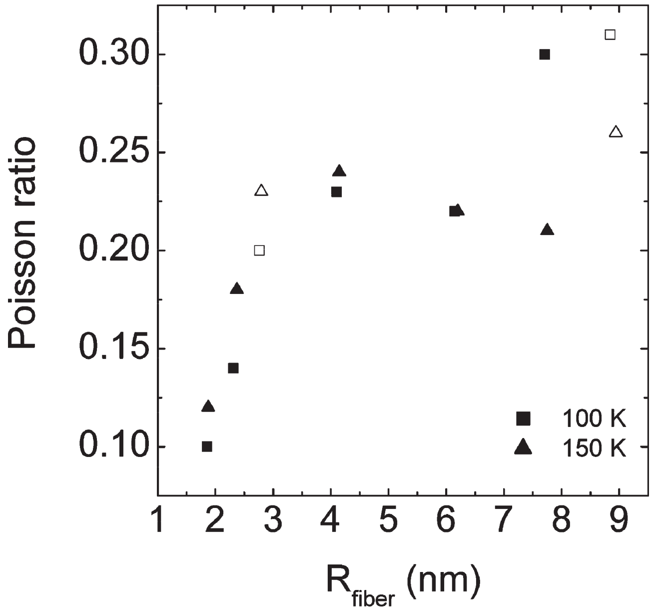

Figure 7. Poisson's ratio increases as the fiber radius increases at 100 and 150 K. Symbols are the same as in Figure 5. Solid symbols represent systems with chain length C100; open symbols represent systems with chain length C150.

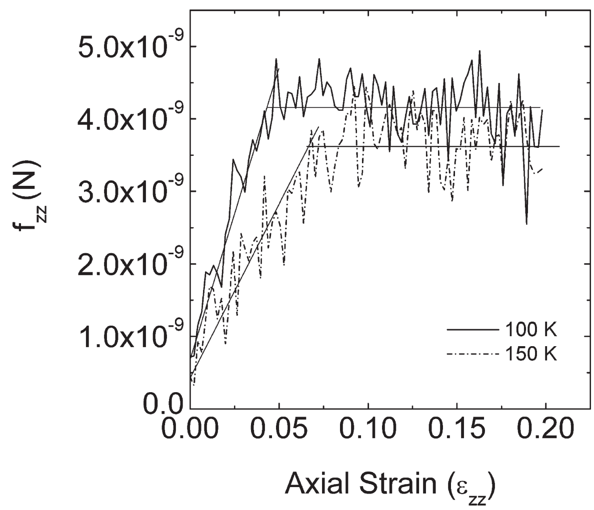

Figure 8. Averaged axial force vs axial strain response for plastic deformation of a fiber (C_{100}, $R_{\text{fiber}} = 4.1$ nm at 100 K) at 100 and 150 K at a strain rate of 10^{9} s^{-1}.

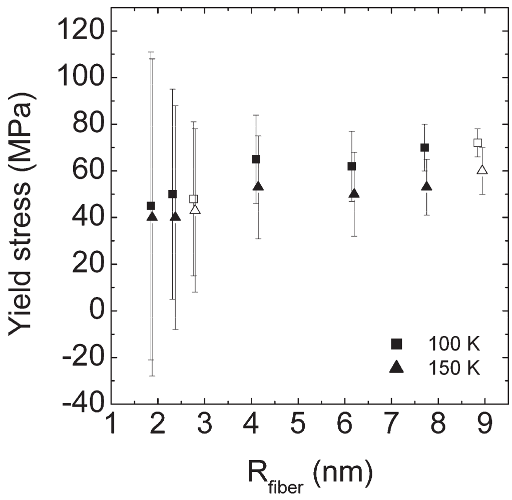

Figure 9. Yield stress as a function of fiber radius at 100 and 150 K determined at a strain rate of 10^9 s^{-1}. Key: solid symbols, C100; open symbols, C150.

tified by ξ. According to our model (Figure 6b), the distance over which these relaxations occur can be as large as twice the radius of gyration of the chain ($R_{g,bulk} = 1.6$ nm for C100) at 100 K. The thickness of this layer decreases to 2.8 nm at 150 K and 1.0 nm at 200 K. For amorphous polymer thin films of PS or PMMA on PDMS substrates, Stafford et al.[30] estimated a surface layer of thickness 2 nm with an elastic modulus lower than that of the corresponding bulk polymer. Sharp et al.[46] suggested the existence of a liquidlike surface layer with thickness of 3−4 nm, from studies of 10 nm and 20 nm diameter gold spheres embedded into a PS surface. They also estimated the thickness of this layer to be 5±1 nm from ellipsometry measurements.[46] These estimates compare favorably with our results for ξ of simulated amorphous PE.

The decrease in the thickness of the mechanically effective surface layer with increasing temperature is similar to the behavior that we noted previously for the cooperatively rearranging region (CRR), which we used to explain trends in the glass transition temperature as a function of PE nanofiber diameter.[24] It is well established that structural relaxation in amorphous polymers occurs through cooperative rearrangements that involve larger domains of material as the temperature is reduced through the glass transition.[47] Similar behavior can be expected for ξ. However, the ξ determined here for the mechanically effective surface layer are larger than those of the CRR for thermal relaxations, for which we previously calculated values of 1.0, 0.75, and 0.58 nm at 100, 150, and 200 K, respectively.[24] To the best of our knowledge, there is no study in the literature that compares the thickness ξ of the mechanically effective surface layer with that of the CRR. Our results show that cooperative mechanical displacement occurs over a larger distance (ξ) than thermal rearrangements (CRR), requiring the involvement of more repeat units. Although mechanical loads can be transmitted along an appreciable fraction of the entire chain length, thermal relaxations take place over a smaller number of repeat units, resulting in smaller surface layer thickness. Although the two-layer composite model appears to be a reasonable approximation to explain deviations in T_g[24] and in E from bulk material, this model is nevertheless simplistic, and its estimates are certainly approximate. More complex models may need to be devised in order to rationalize quantitatively the complex physics underlying thermal and mechanical properties of nanofibers with those of the bulk and thin films.

We also computed the Poisson's ratio ν of the PE nanofibers as a function of fiber size and temperature directly from the ratio of radial and axial strains. As Figure 7 shows, ν decreases from 0.3 to 0.1 nm as R_{fiber} decreases from 8.8 to 1.8 nm. The Poisson's ratio of large fibers is comparable to the Poisson's ratio of a typical glassy polymer of ~0.3. The small nanofibers exhibited Poisson's ratios similar to porous composite materials such as cork ($\nu \sim 0$) and concrete ($\nu \sim 0.2$). The low Poisson's ratio and reduced lateral contraction of the smallest glassy fibers may be partially attributable to the increased volume fraction of the comparatively mobile, mechanically effective surface layer in these nanoscale fibers.

C. Plastic Deformation. Plastic deformation (e.g., yielding and subsequent fracture) of the nanofibers may have important consequences for the mechanical performance of the individual nanofibers as well as the nonwoven mats comprising such fibers. For this reason, we investigated the large-strain behavior of several nanofibers under uniaxial tension to determine the yield stress and its possible dependence on temperature and fiber diameter.

Figure 8 shows such a force−strain response, up to and beyond the onset of plastic deformation. Although the signal-to-noise ratio of the force and strain data points is inevitably low, the applied yield force f_y can be estimated (see B. Simulation Methods). Yield force is then normalized by the cross-sectional area to compute yield stress σ_y. Figure 9 shows yield stress σ_y as a function of fiber radius ranging from 40 to 72 MPa at 100 and 150 K and a strain rate of 10^9 s^{-1}. Experimentally available measurements of yield strength for PE range between 9.6 and 33.0 MPa at room temperature.[48] However, these measurements are invariably for semicrystalline PE, in which the yield is predominantly due to crystallographic slip along the {100}⟨001⟩ slip system,[49] which is activated at lower stress rather than yield within the amorphous component. Thus, our results are not necessarily inconsistent with the experimental data. For a more direct comparison, we determined σ_y by simulation for an amorphous bulk PE undergoing tensile deformation at a strain rate of 10^9 s^{-1} and obtained $\sigma_y = 150$ and 120 MPa at 100 and 150 K, respectively. This tensile yield stress is ~25% lower than that reported by Capaldi et al. for simulated yield strength in compression, using the same force field and comparable strain rates.[37] Vorselaars et al. have also reported about 25% lower yield stress in tension than in compression for their simulations of a bulk polystyrene glass.[50] Thus, the yield stress for these fibers ranges from one-third to one-half that of the corresponding bulk values; this suggests that the surface layer plays a significant role in facilitating plastic deformation. Finally, although our simulations indicate that the average yield stress increases mildly with increasing fiber radius and decreasing temperature, the error bars associated with identification of the yield point in simulated force−strain responses, particularly for fibers of radii less than 4 nm, preclude identification of size-dependent trends in strength over this range of fiber radii.

Discussion and Conclusions

Through direct MD simulations of the uniaxial loading response for amorphous PE nanofibers, we have calculated elastic and plastic properties of individual fibers as a function of fiber radius and temperature. Young's moduli of these nanofibers are found to decrease with decreasing fiber radius, which is counter to experimental results available for semicrystalline and amorphous polymer fibers.[6−17] However, the experimental fiber diameters for which an increase in E with decreasing fiber diameter has been reported are much larger (e.g., 700 nm for PCL[12]) than the simulated nanofibers (3.7 nm < d < 17.7 nm) presented in this work. More importantly, to our knowledge, all the nanofibers that were tested experimentally are semicrystalline, with the notable exception of PS,[17] while all our simulated nanofibers are completely amorphous. In one study of PCL nanofibers, crystallinity and molecular orientation were found to increase with decreasing fiber diameter, based on wide-angle X-ray scattering experiments and draw ratio calculations, which was correlated in turn with the increase in stiffness of PCL nanofibers with decreasing radius.[12] In contrast, Arinstein et al. reported that crystallinity and orientation in nylon-6,6 nanofibers showed only a modest, monotonic increase[16] that could not be correlated with the dramatic increase in Young's modulus observed with decreasing fiber diameter; the authors concluded that confinement on a supramolecular length scale must be responsible for this increase.[16] In the case of amorphous PS fibers in the range 410 nm < d < 4 μm, the increase in shear elastic modulus was attributed to molecular chain alignment arising from the extensional flow of the electrospinning process itself;[17] as mentioned earlier, our simulated nanofibers do not exhibit any significant molecular level orientation. Thus, while we cannot account for the roles of crystallinity and molecular orientation in the experimental fiber studies, we can infer from our results that the primary consequence of diameter reduction in the smallest fibers (ca. 5−20 nm diameter) is a reduction of elastic modulus, Poisson's ratio, and yield stress of these fibers as compared to the bulk counterparts, all of which we attribute to an intrinsically mobile surface layer. Significantly, our results for decreasing stiffness with decreasing fiber diameter are consistent with simulations of nanoscale cantilevered free-standing film[25,26] and adhered thin film simulations[27] as well as with experiments on adhered thin films of amorphous glassy polymers[30−32] of comparable (< 50 nm) physical dimensions.

The simple two-layer composite material model proposed herein successfully captures the dependence of E on fiber radius and temperature. The mechanically effective surface layer over which the load is transmitted apparently entails the cooperative motion of large portions of the chains (of C100 or C150). The thickness of this mechanically effective surface layer exceeds the length scale for thermal rearrangement, which requires the cooperative motion of only 3−4 CH_2 units. Although these estimates are approximate in view of the simplicity of the composite model that was used, such a framework rationalizes the evidence for decreasing elastic modulus with decreasing fiber diameter.

Continuum theory suggests that finite stress, which is a consequence of surface tension, exists on nanofibers prior to deformation. The results presented here provide numerical evidence that surface tension calculated from the virial equation for stress is in agreement with continuum mechanics predictions[40] and experimental results.[42] It is notable that the Young−Laplace equation is capable of capturing the finite surface tension effect on these fibers of nanoscale (< 10 nm) radius.

Acknowledgment. This work was supported by the DuPont-MIT Alliance and DuPont Young Professor Award (K.J.V.V.).

References and Notes

(1) Barhate, R. S.; Ramakrishna, S. *J. Membr. Sci.* **2007**, *296*, 1–8.
(2) Martins, A.; Araujo, J. V.; Reis, R. L.; Neves, N. M. *Nanomedicine* **2007**, *2*, 929–942.
(3) Liang, D.; Hsiao, B.; Chu, B. *Adv. Drug Delivery Rev.* **2007**, *59*, 1392–1412.
(4) Yeo, L. Y.; Friend, J. R. *J. Exp. Nanosci.* **2006**, *1*, 177–209.
(5) Burger, C.; Hsiao, B.; Chu, B. *Annu. Rev. Mater. Res.* **2006**, *36*, 333–368.
(6) Wang, M.; Jin, H. J.; Kaplan, D. L.; Rutledge, G. C. *Macromolecules* **2004**, *37*, 6856–6864.
(7) Inai, R.; Kotaki, M.; Ramakrishna, S. *Nanotechnology* **2005**, *16*, 208–213.
(8) Bellan, L. M.; Kameoka, J.; Craighead, H. G. *Nanotechnology* **2005**, *16*, 1095–1099.
(9) Tan, E. P. S.; Goh, C. N.; Sow, C. H.; Lim, C. T. *Appl. Phys. Lett.* **2005**, *86*, 073115-1−073115-3.
(10) Tan, E. P. S.; Ng, S. Y.; Lim, C. T. *Biomaterials* **2005**, *26*, 1453–1456.
(11) Chew, S. Y.; Hufnagel, T. C.; Lim, C. T.; Leong, K. W. *Nanotechnology* **2006**, *17*, 3880–3891.
(12) Wong, S. C.; Baji, A.; Leng, S. *Polymer* **2008**, *49*, 4713–4722.
(13) Li, L.; Bellan, L. M.; Craighead, H. G.; Frey, M. W. *Polymer* **2006**, *47*, 6208–6217.
(14) Shin, M. K.; Kim, S. I.; Kim, S. J.; Kim, S. K.; Lee, H.; Spinks, G. M. *Appl. Phys. Lett.* **2006**, *89*, 231929-1−231929-3.
(15) Zussman, E.; Burman, M.; Yarin, A. L.; Khalfin, R.; Cohen, Y. *J. Polym. Sci., Part B: Polym. Phys.* **2006**, *44*, 1482–1489.
(16) Arinstein, A.; Burman, M.; Gendelman, O.; Zussman, E. *Nat. Nanotechnol.* **2007**, *2*, 59–62.
(17) Ji, Y.; Li, B.; Ge, S.; Sokolov, J. C.; Rafailovich, M. H. *Langmuir* **2006**, *22*, 1321–1328.
(18) Keddie, J. L.; Jones, R. A. L.; Cory, R. A. *Europhys. Lett.* **1994**, *27*, 59–64.
(19) Keddie, J. L.; Jones, R. A. L. *Isr. J. Chem.* **1995**, *35*, 21–26.
(20) Fryer, D.; Nealey, P. F.; de Pablo, J. J. *Macromolecules* **2000**, *33*, 6439–6447.
(21) Forrest, J. A.; Dalnoki-Veress, K.; Dutcher, J. R. *Phys. Rev. E* **1997**, *56*, 5705–5716.
(22) Ellison, C. J.; Torkelson, J. M. *Nat. Mater.* **2003**, *2*, 695–700.
(23) Torres, J. A.; Nealey, P. F.; de Pablo, J. J. *Phys. Rev. Lett.* **2000**, *85*, 3221–3224.
(24) Curgul, S.; Van Vliet, K. J.; Rutledge, G. C. *Macromolecules* **2007**, *40*, 8483–8489.
(25) Bohme, T. R.; de Pablo, J. J. *J. Chem. Phys.* **2002**, *116*, 9939–9951.
(26) Van Workum, K.; de Pablo, J. J. *Nano Lett.* **2003**, *3*, 1405–1410.
(27) Yoshimoto, K.; Jain, T. S.; Nealey, P. F.; de Pablo, J. J. *J. Chem. Phys.* **2005**, *122*, 144712-1−144712-6.
(28) Vao-soongnern, V.; Doruker, P.; Mattice, W. L. *Macromol. Theory Simul.* **2000**, *9*, 1–13.
(29) Vao-soongnern, V.; Mattice, W. L. *Langmuir* **2000**, *16*, 6757–6758.
(30) Stafford, C. M.; Harrison, C.; Beers, K. L.; Karim, A.; Amis, E. J.; VanLandingham, M. R.; Kim, H. C.; Volksen, W.; Miller, R. D.; Simonyi, E. E. *Nat. Mater.* **2004**, *3*, 545–550.
(31) Stafford, C. M.; Vogt, B. D.; Harrison, C.; Julthongpiput, D.; Huang, R. *Macromolecules* **2006**, *39*, 5095–5099.
(32) Zhao, J. H.; Kiene, M.; Hu, C.; Ho, P. S. *Appl. Phys. Lett.* **2000**, *77*, 2843–2845.
(33) Plimpton, S. J. *J. Comput. Phys.* **1995**, *117*, 1–19.
(34) Paul, W.; Yoon, D. Y.; Smith, G. D. *J. Chem. Phys.* **1995**, *103*, 1702–1709.
(35) Bolton, K.; Bosio, S. B. M.; Hase, W. L.; Schneider, W. F.; Hass, K. C. *J. Phys. Chem. B* **1999**, *103*, 3885–3895.
(36) In't Veld, P. J.; Rutledge, G. C. *Macromolecules* **2003**, *36*, 7358–7365.
(37) Capaldi, F. M.; Boyce, M. C.; Rutledge, G. C. *Polymer* **2004**, *45*, 1391–1399.
(38) Manevitch, O. L.; Rutledge, G. C. *J. Phys. Chem. B* **2004**, *108*, 1428–1435.
(39) http://www.povray.org.
(40) Adamson, A. W. In *Physical Chemistry of Surfaces*, 3rd ed.; Wiley and Sons: New York, 1976; Chapter 1.
(41) In't Veld, P. J.; Hutter, M.; Rutledge, G. C. *Macromolecules* **2006**, *39*, 439–447.
(42) Brandrup, J.; Immergut, E. H.; Grulke, E. A.; Abe, A.; Bloch, D. R. In *Polymer Handbook*, 4th ed.; John Wiley & Sons: New York, 1999.
(43) Capaldi, F. M.; Boyce, M. C.; Rutledge, G. C. *Phys. Rev. Lett.* **2002**, *89*, 175505-1−175505-4.
(44) Fakhraai, Z.; Forrest, J. A. *Science* **2008**, *319*, 600–604.

(45) Peter, S.; Meyer, H.; Baschnagel, J. *J. Phys: Condens. Matter* **2007**, *19*, 2051159 (11 pp).
(46) Sharp, J. S.; Teichroeb, J. H.; Forrest, J. A. *Eur. Phys. J. E* **2004**, *15*, 473–487.
(47) Del Gado, E.; Ilg, P.; Kroeger, M.; Oettinger, H. C. *Phys. Rev. Lett.* **2008**, *101*, 095501 (4 pp).
(48) Avallone, E. A.; Baumeister, T., III In *Mark's Standard Handbook for Mechanical Engineers*, 10th ed.; McGraw-Hill: New York, 1996.
(49) Kazmierczak, T.; Galeski, A.; Argon, A. S. *Polymer* **2005**, *46*, 8926–8936.
(50) Vorselaars, B.; Lyulin, A. V.; Michels, M. A. J. *J. Chem. Phys.* **2009**, *130*, 074905 (14 pp).